Macromolecular and electrical coupling between inner hair cells in the rodent cochlea

Philippe Jean[1,2,3,4,#], Tommi Anttonen[1,2,5,#], Susann Michanski[2,6,7], Antonio MG de Diego[8], Anna M. Steyer[9,10], Andreas Neef[11], David Oestreicher[12], Jana Kroll[2,4,6,7], Christos Nardis[9,10], Tina Pangršič[2,12], Wiebke Möbius[9,10], Jonathan Ashmore[8], Carolin Wichmann[2,6,7,13*], and Tobias Moser[1,2,3,5,10,13*]

[1]*Institute for Auditory Neuroscience and InnerEarLab, University Medical Center Göttingen, Göttingen, Germany*

[2]*Collaborative Research Center 889, University of Göttingen, Göttingen, Germany*

[3]*Auditory Neuroscience Group, Max Planck Institute of Experimental Medicine, Göttingen, Germany*

[4]*Göttingen Graduate School for Neurosciences and Molecular Biosciences, University of Göttingen, Göttingen, Germany*

[5]*Synaptic Nanophysiology Group, Max Planck Institute of Biophysical Chemistry, Göttingen, Germany*

[6]*Molecular Architecture of Synapses Group, Institute for Auditory Neuroscience and InnerEarLab, University Medical Center Göttingen, Göttingen, Germany*

[7]*Center for Biostructural Imaging of Neurodegeneration, Göttingen, Germany*

[8]*UCL Ear Institute and Department of Neuroscience, Physiology and Pharmacology, University College London, London, UK*

[9]*Electron Microscopy Core Unit, Department of Neurogenetics, Max Planck Institute of Experimental Medicine, Göttingen, Germany*

[10]*Center for Nanoscale Microscopy and Molecular Physiology of the Brain, University of Göttingen, Göttingen, Germany*

[11]*Neurophysics laboratory, Campus Institute for Dynamics of Biological Networks, University of Göttingen, Göttingen, Germany*

[12]*Experimental Otology Group, Institute for Auditory Neuroscience, InnerEarLab, and Department of Otolaryngology, University Medical Center Göttingen, Göttingen, Germany*

[13]*Multiscale Bioimaging Cluster of Excellence (MBExC), University of Göttingen, Göttingen, Germany*

[#]These authors contributed equally to this work

[*]Corresponding authors

Short title: Coupling among cochlear inner hair cells

Abstract

Inner hair cells (IHCs) are the primary receptors for hearing. They are housed in the cochlea and convey sound information to the brain via synapses with the auditory nerve. IHCs have been thought to be electrically and metabolically independent from each other. We report that, upon developmental maturation, 30% of the IHCs are electrochemically coupled in 'mini-syncytia'. This coupling permits transfer of fluorescently-labeled metabolites and macromolecular tracers. The membrane capacitance, Ca^{2+}-current, and resting current increase with the number of dye-coupled IHCs. Dual voltage-clamp experiments substantiate low resistance electrical coupling. Pharmacology and tracer permeability rule out coupling by gap junctions and purinoceptors. 3D-electron-microscopy indicates instead that IHCs are coupled by membrane fusion sites. Consequently, depolarization of one IHC triggers presynaptic Ca^{2+}-influx at active zones in the entire mini-syncytium. Based on our findings and modeling, we propose that IHC-mini-syncytia enhance sensitivity and reliability of cochlear sound encoding.

Introduction

The well-established *neuron doctrine* of Ramón y Cajal states that neurons operate as independent cellular entities that communicate at specific contact points, presently known as chemical and electrical synapses[1]. Although cell-cell fusion is a normal part of the development of several non-neuronal cell types, the reticular theory of Gerlach and Golgi stating that the nervous system is a single continuous network of neural cells is considered obsolete. However, several studies indicate that neural cells are capable of fusion both under physiological and pathological conditions. For example, direct neuron-neuron fusion has been reported in *C. elegans*[2] but, in the mammalian nervous system, the prevalence and possible physiological significance of neuron-neuron fusion is less clear[3].

In contrast, neural communication via gap junction (GJ)-coupling is well established[4]. GJs are formed by connexins that connect the cytoplasm of two cells together and allow the propagation of electrical signals and molecules up to ~1 kDa in size[5]. Being at the core of electrical synapses, GJs are essential for synchronized spiking activity in the central nervous system[6]. In mammalian sensory systems, GJs play several important roles: GJ-coupling between retinal photoreceptors shapes visual sensitivity[7], while in the olfactory system GJs contribute to the lateral excitation of mitral cells[8].

In the cochlea, GJs between glial-like supporting cells (SCs) are critical for normal hearing, whereas inner hair cells (IHCs) are assumed to lack electrochemical coupling[9]. IHCs are the mechanosensitive receptors of hearing that transform sound born vibrations into electrical activity of the spiral ganglion neurons (SGNs). Each SGN is believed to innervate and receive input from a single IHC[10]. First steps of auditory sensory processing already occur in the cochlea: Due to its tonotopical organization, SGNs innervating IHCs of the apical coil encode low-frequency sounds, while those of the basal coil encode high-frequency sounds[11]. Here, we

demonstrate that in rodents, approximately one third of IHCs undergo homotypic macromolecular and low-resistance electrical coupling upon cochlear maturation, putatively via IHC-IHC fusion. The resulting IHC mini-syncytia form small receptive fields that pool signals and improve sensitivity and reliability of auditory coding, yet maintain its frequency resolution.

Results

Spread of dyes between rodent IHCs indicates macromolecular coupling

Coupling between IHCs was observed as dye-spread into neighboring IHCs (Fig. 1) in two independent laboratories combining whole-cell patch-clamp recordings with fluorescence imaging of IHCs from apical (~4-8 kHz) and mid-cochlear (~10-16 kHz) regions in 2-13 week-old mice (C57BL/6J/6N and CD1 backgrounds; Fig. 1a). Such dye-coupling among IHCs was unlikely to have artificially resulted from cellular damage in the *ex vivo* preparation. It was not only found in IHCs of the excised organ of Corti (Lucifer yellow, LY, ~0.4 kDa, Fig. 1a,c,d,d'), but also in a temporal bone preparation (Oregon-Green-Bapta-5N, OGB5N, ~1 kDa, Fig. 1b,b'). The coupling is also metabolic as fluorescently labeled glucose was detected diffusing between IHCs (Fig. S1a). In addition to the spread of low molecular tracers, also a larger tetramethylrhodamine (TAMRA)-conjugated CtBP2 binding peptide (~4.4 kDa) diffused between IHCs (Fig. 1e-f'; Movies S1-3) as well as even large fluorophore-conjugated antibodies (~150 kDa; Fig. 1g; Fig. S1b), indicating that the coupling mechanism, unlike GJs (size limit: ~1 kDa)[9], supports the exchange of macromolecules. Moreover, IHC macromolecular coupling is not limited to mice, as spreading of TAMRA-peptide was also observed in low-frequency (~200-450 Hz) as well as high-frequency (~24-48 kHz) IHCs of 2-6-week-old Mongolian gerbils (Fig. S2). Therefore, rodent IHCs are capable of forming mini-syncytia in which the receptor cells undergo diffusional exchange of molecules.

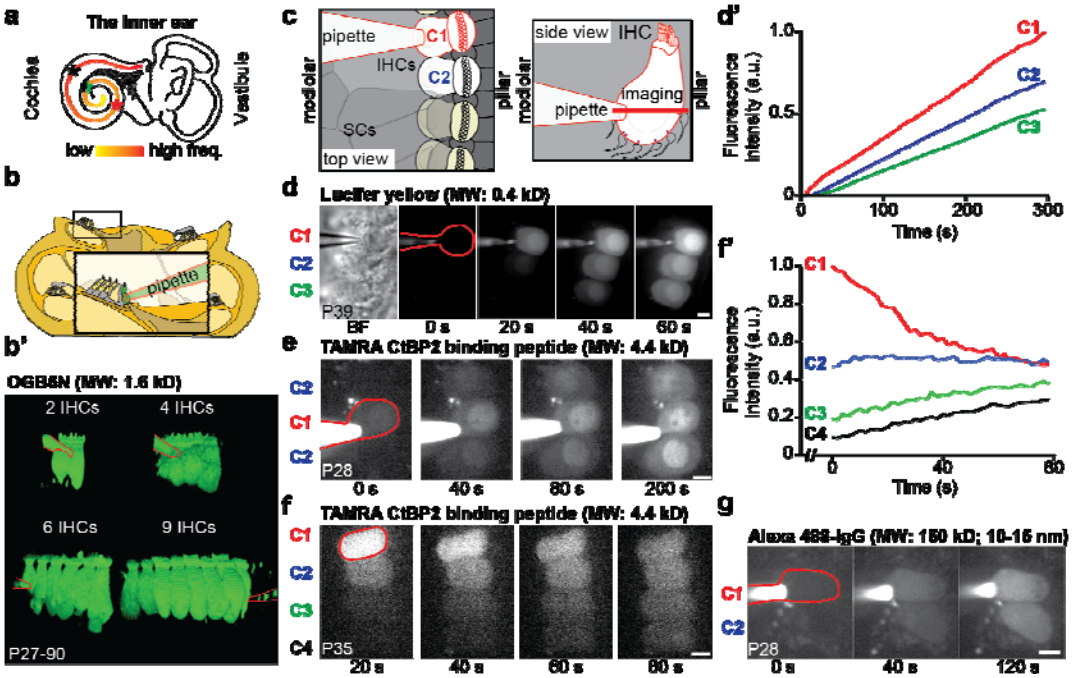

Figure 1. Macromolecular coupling between mature mouse IHCs. (a) Illustration of the cochlea with the tonotopic map color-coded for frequency and approximate positions of patching indicated with asterisks (red = mouse temporal bone preparation; green = mouse excised organ of Corti; black = gerbil excised organ of Corti (Fig. S2)). **(b)** Drawing illustrating the temporal bone preparation, where the bone covering the apical turn is removed. **(b')** 3D view of OGB5N fluorescence between 2,4,6, and 9 coupled IHCs, with pipette delineated in red. **(c)** Drawings illustrating the excised organ of Corti with SCs removed to allow patching of one IHC (C1, outlined in red in panels d,e,f, and g), loaded IHCs in white (C1,C2), imaging plane as red bar. **(d)** Time series of Lucifer yellow loading into 3 coupled IHCs, shown in bright field (BF) on the left. **(d')** Normalized fluorescence intensities over time from d. **(e)** Time series of TAMRA loading into 3 coupled IHCs. **(f)** TAMRA-peptide diffusion between 4 coupled IHCs after retracting the patch-pipette from C1. **(f')** Normalized fluorescence intensities over time from f. **(g)** Time series of Alexa 488-IgG loading in 2 coupled IHCs. *Abbreviations: a.u.*, arbitrary units; *IHC*, inner hair cell; *MW*, molecular weight; *P*, postnatal day; *SC*, supporting cell. *Scale bar* = 5 µm in d,e,f,g.

IHC coupling is established during late postnatal development

The prevalence of dye-coupling among mouse IHCs increased during postnatal IHC maturation (Fig. 2a-c). Shortly after hearing onset (P14-18)[12] only 2% of patched IHCs were dye-coupled (Fig. 2a). In mice aged P21-28, 6.6% of IHCs formed 'mini-syncytia' of up to 5 IHCs (Fig. 2b). In P30-45 mice, 29% of IHCs were coupled and the distribution of IHCs coupled in the mini-syncytia (up to 7 IHCs, Fig. 2c and Fig. S1b) significantly differed from

P21-28 (Kolmogorov-Smirnov test, $p < 0.00001$). In temporal bone preparations, 33% of IHCs were coupled in P26-100 mice, with up to 9 IHCs in a mini-syncytium (Fig. S3).

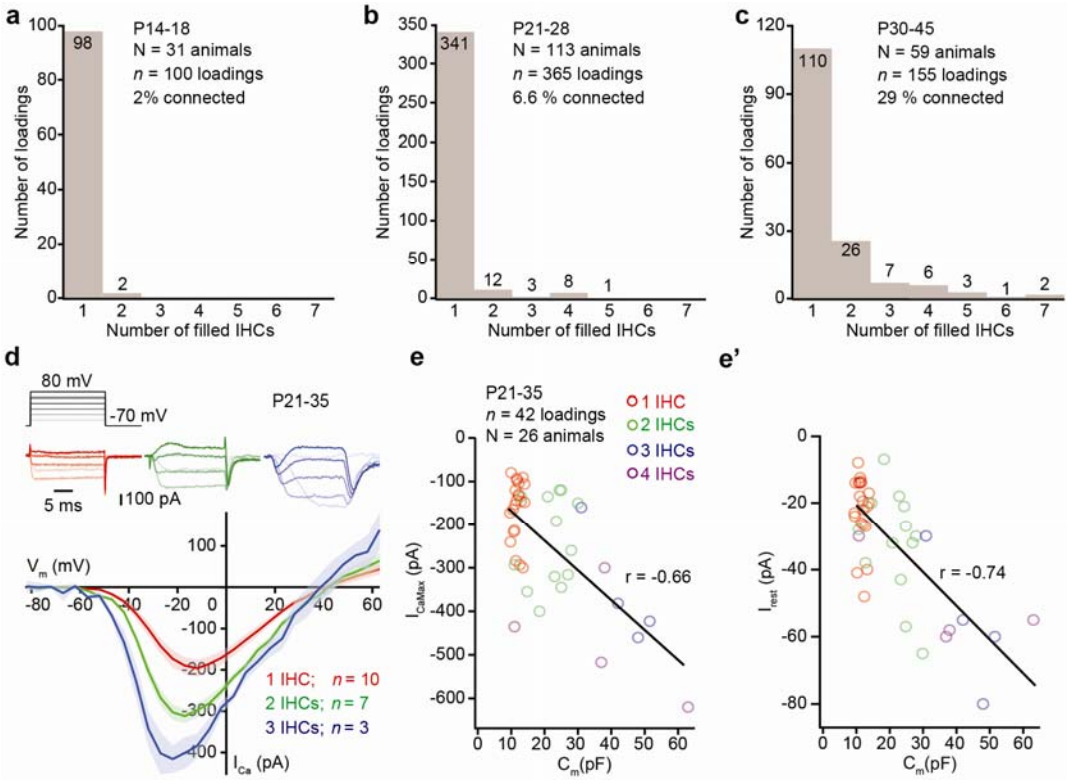

Figure 2. IHC coupling is age-dependent and electrical. (a-c) Histograms displaying the number of dye-filled IHCs per loading at 3 different developmental stages. **(d)** Representative whole-cell Ca^{2+}-currents ($[Ca^{2+}]_e$ = 5 mM) of a single IHC (red), 2 (green), and 3 (blue) coupled IHCs under step depolarizations from -70 to 80 mV at P21-35 (as in 2e,f). Current-voltage relationships (IVs) in single and dye-coupled IHCs with mean (line) ± S.E.M. (shaded areas). **(e-e')** Scatter plots and line fits relating I_{CaMax} (e) and I_{rest} (e') currents against C_m values according to the number of dye-coupled IHCs. *Abbreviations:* C_m, membrane capacitance; I_{CaMax}, maximal Ca^{2+}-current; *IHC*, inner hair cell; I_{rest}, resting current.

Low resistance electrical connections between coupled IHCs

Macromolecular coupling is accompanied by low resistance electrical coupling of IHCs. Indeed, the maximal voltage-gated Ca^{2+}-influx (I_{CaMax}) and resting currents (I_{rest}) increase with the number of dye-filled IHCs (Fig. 2d,e,e', Fig. S2b). Both parameters were significantly larger for mini-syncytia of 3 and 4 dye-coupled IHCs than for single IHCs (1 IHC: I_{CaMax} = -161 ± 15 pA, I_{rest} = -22.05 ± 2.23 pA, n = 21 (data taken from Jean *et al*., 2018 where similar recording

conditions were used); 2 IHCs: I_{CaMax} = -241 ± 28 pA, I_{rest} = -32.15 ± 4.39 pA, *n* = 13; 3 IHCs: I_{CaMax} = -356 ± 67 pA, I_{rest} = -56.25 ± 10.28 pA, *n* = 4; 4 IHCs: I_{CaMax} = -482 ± 68 pA, I_{rest} = -50.75 ± 6.99 pA, *n* = 4 recordings; mean ± S.E.M, Dunn-Holland-Wolfe non-parametric multiple comparison test, $p < 0.05$ for 3 IHCs and 4 IHCs vs. 1 IHC). Interestingly, the strength of IHC coupling varied as also indicated by the variable spread of the TAMRA peptide (Fig. S1c,c'). Strongly dye-coupled IHCs, showing a rapid dye-spread, exhibited fast monophasic I_{Ca} activation kinetics. In the rare case of weakly dye-coupled IHCs, showing slow dye-spread, I_{Ca} exhibited a multiphasic activation, probably due to poorer voltage-clamp of the coupled IHCs via a larger intercellular resistance (Fig. S1d,d' and Fig. S2b). Likewise, membrane capacitance (C_m) estimates, derived from capacitive currents to voltage steps, increased with the number of dye-coupled IHCs again indicating low resistance connections in the majority of the mini-syncytia. As expected, a correlation with C_m was found for I_{CaMax} (r = -0.66, $p < 0.00001$, Fig. 2e) as well as for I_{rest} (Fig 2e', r = -0.74, $p < 0.00001$). In a larger data set combining different $[Ca^{2+}]_e$ (1.3, 2 or 5 mM), correlations of were also found for I_{CaMax} and I_{rest} with C_m (I_{CaMax}, r = -0.66, $p < 0.00001$, I_{rest}, r = -0.64, $p < 0.00001$, P15-51, Fig. S1e,e'). Similar observations were made i) from ruptured-patch recordings from IHCs of the excised apical and basal gerbil organ of Corti (P14-38, Fig. S2), ii) from perforated-patch recordings of mouse IHCs in the excised organ of Corti (*n* = 14 IHCs, $N_{animals}$ = 11, P15-P36), and iii) from ruptured-patch recording of IHCs when only one inner sulcus cell was removed for access of the pipette in the excised apical mouse organ of Corti (*n* = 15 IHCs; $N_{animals}$ = 6, P16-P24, Fig. S4).

In addition, we analyzed the membrane conductance as a function of the number of OGB5N-loaded IHCs in the temporal bone preparation. Using Cs^+ to minimize the conductance of K^+ channel we depolarized the patch-clamped IHCs to various levels (100 ms long depolarizations in 10 mV increments from a holding potential of -60 mV (Fig. S5). The Cs^+ currents increased with the number of dye-filled IHCs, indicating a partial summation over the currents of the coupled IHCs. We note that the recordings underestimate the true currents due to the voltage drop over the pipette series resistance to the patched IHC and due to the junctional

resistance among the coupled cells. In order to quantify this result, we analyzed the membrane slope conductance (G_m) of IHCs at -60 and +20 mV. A significant positive correlation of G_m and the number of coupled cells was observed at both potentials (-60 mV: r = 0.78; +20 mV: r = 0.77, both regression slopes significantly different from 0 at $p < 0.05$; Fig. S6).

The above observations suggest that a coupling mechanism forms low resistance connections between IHCs. For a direct estimation of the junctional resistance (R_J), we performed paired voltage-clamp recordings of junctional currents (I_j, Fig. 3) from IHCs in the excised, apical organ of Corti of 3-5-week-old mice. The first cell, recorded in the ruptured-patch configuration was filled with LY (Fig. 3a,b,g). When recording simultaneously from the neighboring IHC, we observed bidirectional I_j for dye-coupled IHCs (Fig. 3c,d), but not when LY was limited only to the loaded IHC (Fig. 3e-g). The R_J between coupled IHCs ranged from 12 to 75 MOhm (35 ± 20 MOhm, *n* = 3). A model of an electrical circuit equivalent of coupled IHCs with R_J of 10 and 100 MOhm rendered I_j values spanning the ones obtained in the paired recordings of coupled IHCs (Fig. 3h,i).

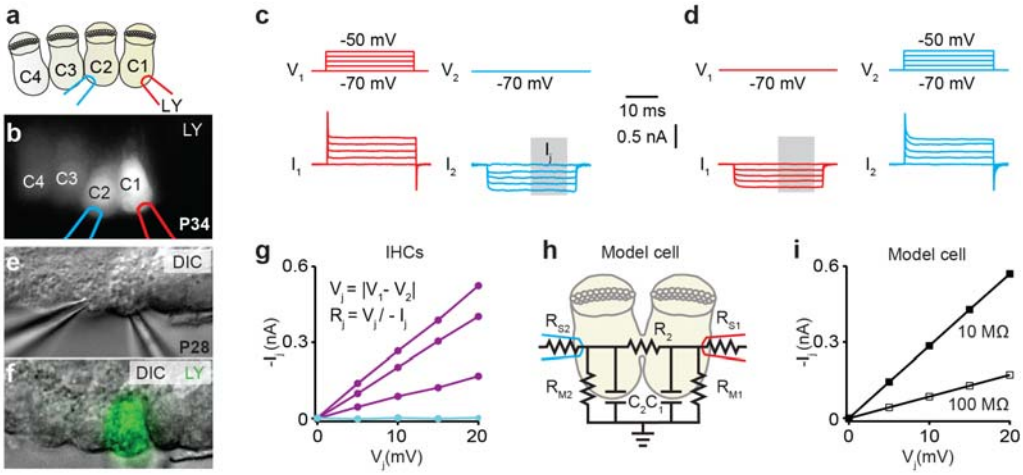

Figure 3. Dual whole-cell voltage-clamp recordings from dye-coupled IHCs reveal bidirectional, low resistance electrical coupling. (a,b) After observing IHC-to-IHC diffusion of LY from the loaded IHC (C1), the second neighboring coupled IHC (C2) was patched with a LY-free pipette (left). **(c,d)** Exemplary dual recording of coupled IHCs (3 recordings in total) demonstrates how depolarizations of one of the IHCs from holding potential (V_H, -70 mV)

produces junctional currents (I_J) in the second IHC held at V_H. **(e,f)** In the absence of dye coupling, no I_J was observed (cyan in g). **(g)** The steep linear I_J-V_J curve indicates a large, ohmic conductance between the dye-coupled IHCs (purple). Negligible conductance is observed in non-coupled IHCs (cyan). **(h)** An electrical circuit equivalent of coupled IHCs (cell capacitance, $C_1 = C_2 = 10$ pF; junctional resistance, $R_J = 10$ MOhm (filled box in i) or 100 MOhm (empty box in i); Cell membrane resistance, $R_{M1} = R_{M2} = 1$ GOhm; Series resistance, $R_{S1} = R_{S2} = 10$ MOhm) (**i**) produces I_J values that frame those of coupled IHCs (compare to g). *Abbreviations:* V_J, junctional voltage difference; I_J, junctional current; *LY*, lucifer yellow.

Pharmacology rules out GJs and P2X7-dependent macropores as an IHC coupling mechanism

The ability of IHC coupling mechanism to support macromolecular and low R_J electrical connectivity strongly argues against well-established mechanisms such as GJs. To further confirm this, we tested whether several blockers of connexins can disrupt IHC coupling. Carbenoxolone (CBX) did not prevent IHC dye-coupling (Fig. 4a) nor changed the observed C_m values (Fig. 4b). Flufenamic acid and 1-octanol, also GJ blockers[13], had no effect either (Fig. S7). However, all three blockers reduced I_{CaMax}, which likely reflects inhibition of Ca^{2+}-channels[14–16] since this effect also occurred in non-coupled IHCs (Fig. 4d,e and Fig. S7c,d,g,h). Likewise, the P2X receptor antagonist suramin that blocks P2X7-dependent, pannexin-containing macropores[17] had no effect on C_m or I_{CaMax} (Fig. S7i-l). These findings exclude GJs and P2X7-dependent macropores as mechanisms underlying IHC coupling.

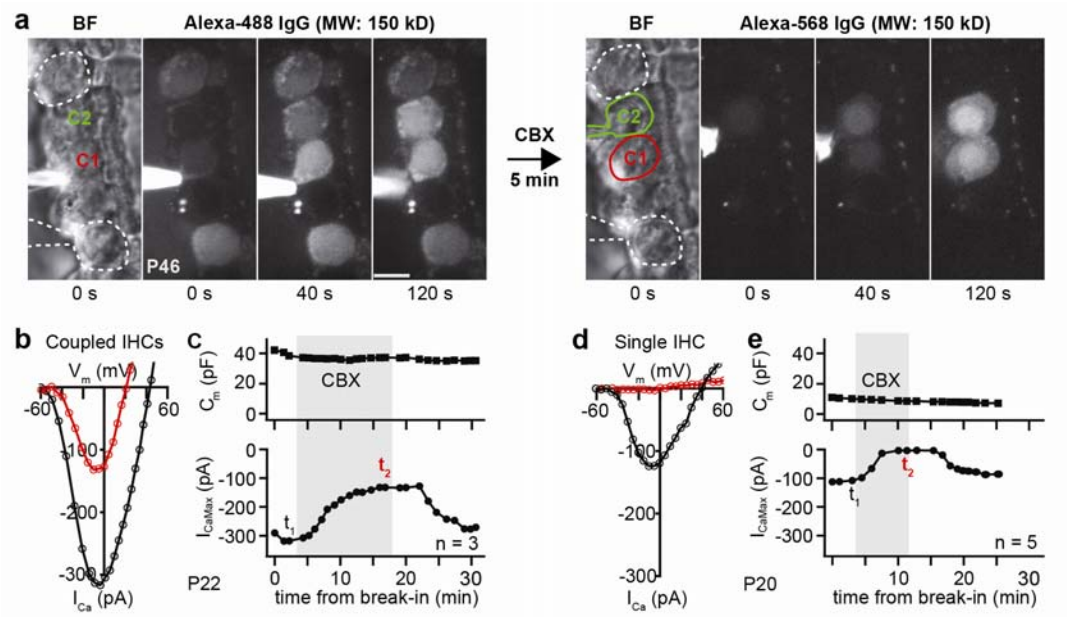

Figure 4. Molecular and electrical IHC coupling is not prevented by the GJ blocker CBX. (a) The left time series of green fluorescence shows how Alexa-488 conjugated antibodies diffuse from the targeted IHC (delineated in red, C1) to the coupled IHC (delineated in green, C2). Two of the surrounding uncoupled IHCs (highlighted by white lines) have previously been loaded with the antibodies. After retracting the pipette, CBX (250 µM) was added to the bath solution five minutes prior to the loading of Alexa-568 conjugated antibodies via patching C2. The right time series of red fluorescence (same length scale as in a) shows that the spread of Alexa-568 conjugated antibodies to C1 is not blocked by CBX. Surrounding SCs, especially inner pillar cells, exhibit auto-fluorescence. **(b-e)** Ca^{2+}-current voltage (IV) curves were obtained by depolarizing IHCs from the holding voltage (-60 mV) with 5 mV steps before and during bath application of GJ blockers. The presence of the blockers is marked with gray in the membrane capacitance (C_m)-time and maximal I_{Ca} (I_{CaMax})-time plots. The recording time points of the presented IV curves are marked with t_1 (for black curve) and t_2 (for red curve) in the I_{CaMax}-time plots. The experiments were stopped when the patched IHC was lost. CBX inhibits I_{Ca} of coupled IHCs without changing C_m, as seen in with single IHCs. *Abbreviations: CBX*, carbenoxolone; *Vm*, membrane voltage. *Scale bar*: a = 5 µm.

3D electron microscopy suggests IHC-IHC fusion as a coupling mechanism

To identify a structural basis for the mechanism of IHC coupling, we employed 3D electron microscopy (focused ion beam–scanning electron microscopy (FIB-SEM): voxel size: 3 nm in x/y and 5 nm in z). We focused our imaging on the perinuclear basolateral membranes of mouse IHCs that appeared to be in contact in more mature preparations (Figs. 5 and 6; Fig. S8; Movie S4). We investigated the membranes of 3 IHCs to their respective neighboring IHCs (neighbors not being included into the IHC count) right after the onset of hearing (2 IHCs from a P15 organ of Corti and 1 IHC from a P16 organ of Corti, n = 3 FIB-SEM runs, $N_{animals}$ = 2) and 3 IHCs after full maturation (2 IHCs from a P34 organ of Corti and 1 IHC from a P37 organ of Corti, n = 3 FIB-SEM runs, $N_{animals}$ = 2). By performing FIB-SEM, we found that SCs usually enwrapped P15/P16 IHCs (Fig. 5a; Fig. 6d). Nonetheless, filopodia-like IHC-protrusions occasionally contacted the neighboring IHC ("filopodial contact", Fig. 5a'; Fig. 6a,d; Table S1). This was further revealed at high resolution using electron tomography of high-pressure frozen/freeze-substituted IHCs (Fig. 6b). However, only one of these contacts appeared to harbor a putative IHC-IHC fusion site with plasma membrane continuity and a cytoplasmic bridge (Fig. S8a, Table 1) reminiscent of tunneling nanotubes[18].

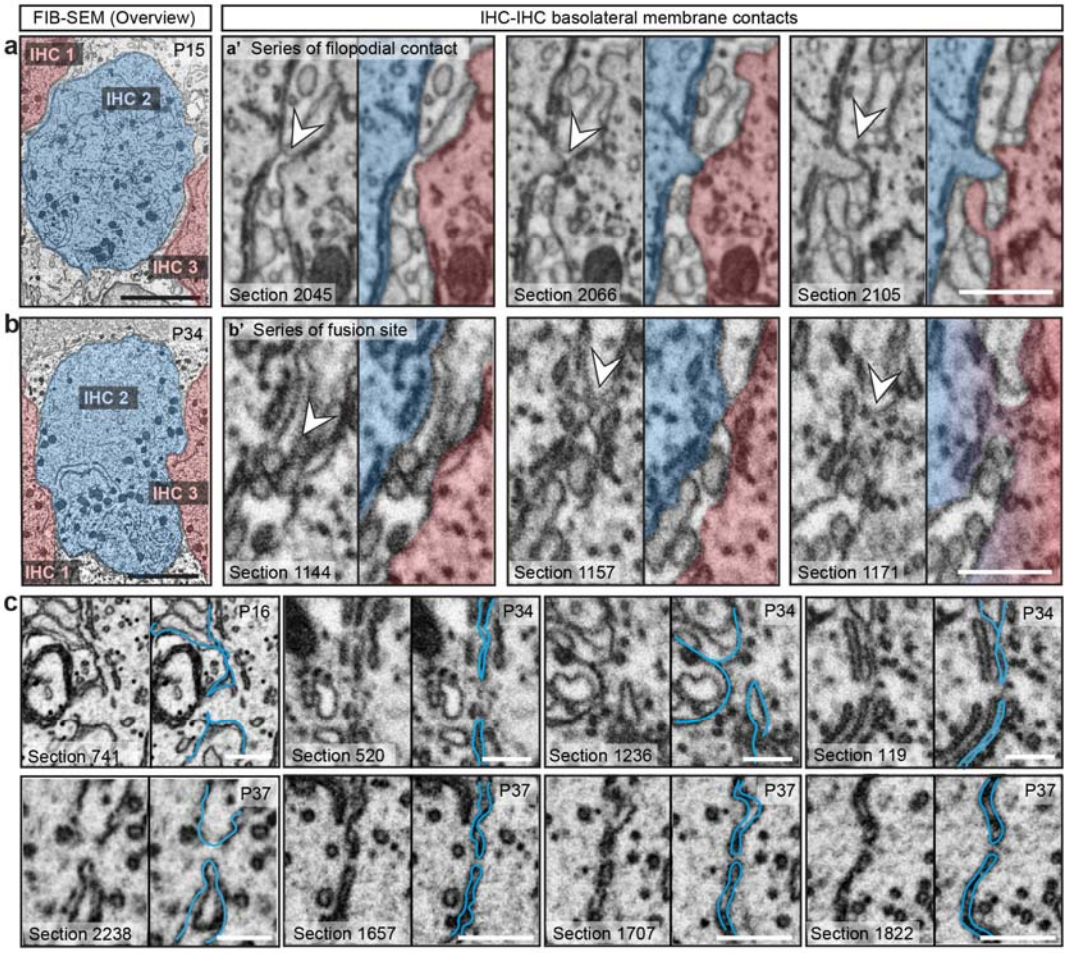

Figure 5. 3D electron microscopy indicates IHC-IHC fusion as a putative basis for IHC coupling. (a-c) FIB-SEM datasets of basolateral membrane contacts between IHCs. **(a)** P15 IHCs are tightly wrapped around by SCs and are separated by a distance ranging from 100 to 648 nm (first section below the nucleus). **(b)** P34 IHCs share prominent flat membrane contacts (blue-red contacts). For each FIB-run we numbered the IHCs, whereby IHC 2 is the full IHC in the centre of the region of interest (highlighted in blue), making contacts to the neighboring IHCs (shown in red). **(a'-c)** Representative micrographs of IHC-IHC contacts. P15 IHCs frequently show filopodia reaching neighboring IHCs **(a')**. **(b')** At P34, some flat membrane contacts appear to include fusion sites with membrane continuity and cytoplasmic bridge (white arrowheads). **(c)** Depicted are the observed putative IHC fusion sites in the P16 and the P34/37 animals. *Abbreviations: FIB-SEM,* focused ion beam-scanning electron microscopy; *IHC,* inner hair cell*; SC,* supporting cells. *Scale bar:* a,b = 5 µm; a',b' = 500 nm; c = 200 nm.

At P34/37, SCs allowed extended membrane contacts between IHCs ("flat contacts", Fig. 5b; Fig. 6a,c',d; Table S1; Movie S4). Some of these contacts featured putative fusion sites with cytoplasmic bridges that occasionally contained ribosomes (Fig. 5b',c; Fig. S8b; Movie S5). The bridges measured, excluding one outlier, 27.9 ± 6.5 nm along the z-axis and 69.3 ± 20.6 nm

in the xy-plane (n = 7 sites in P34/37 IHCs, Table 1). The low number and size of the detected putative fusion sites indicates that this process appears to be self-limiting. In contrast to IHCs, outer hair cells (OHCs) are well separated by SCs. Using serial block face-scanning electron microscopy we did not find direct contacts between P22 OHCs in 34 cases studied (Fig. S9; Movie S6).

Age group	Total *N* of contacts	Filopodial contact		Flat contact		Fusion site		
		Av. length, z	*N*	Av. length, z	*N*	Av. length, z	Av. length, xy	*N*
P15/16	36	114 ± 17.4 nm	32	42.3 ± 3.70 nm	3	35.0 nm	136 nm	1
P34/37	23	198± 7.50 nm	2	1.69 ± 0.57 µm	14	27.9 ± 6.53 nm	69.3 ± 20.6 nm	7

Table 1. Summary of the contact site quantification of the FIB-SEM datasets. Summary of the total number of contacts, of filopodial contacts, flat contacts and putative fusion sites as well as of their average length in z-plane. Note, that we excluded the putative fusion site depicted in Fig. 5c, from the statistics of the P34 data as an outlier, as the z-measurements of 535 nm clearly exceeds 1.5 times the interquartile range above the third quartile (75th percentile). Further, the maximum extent of the cytoplasmic bridge of putative fusion sites was measured in the xy-plane using 3dmod, as indicated in Table S1, and averaged. For the age-group of P15/16 only 1 example for a fusion site was found and the respecting values are listed in the Table. Data are presented as mean ± S.E.M.. P15/16: n = 3 FIB-runs (2 FIB-runs from P15, 1 FIB-run from P16) each with 1 full IHC and the respective contacts to neighboring IHCs, $N_{animals}$ = 2. P34/37: n = 3 FIB-runs (2 FIB-runs from P34, 1 FIB-run from P37) each with 1 full IHC and the respective contacts to neighboring IHCs, $N_{animals}$ = 2.

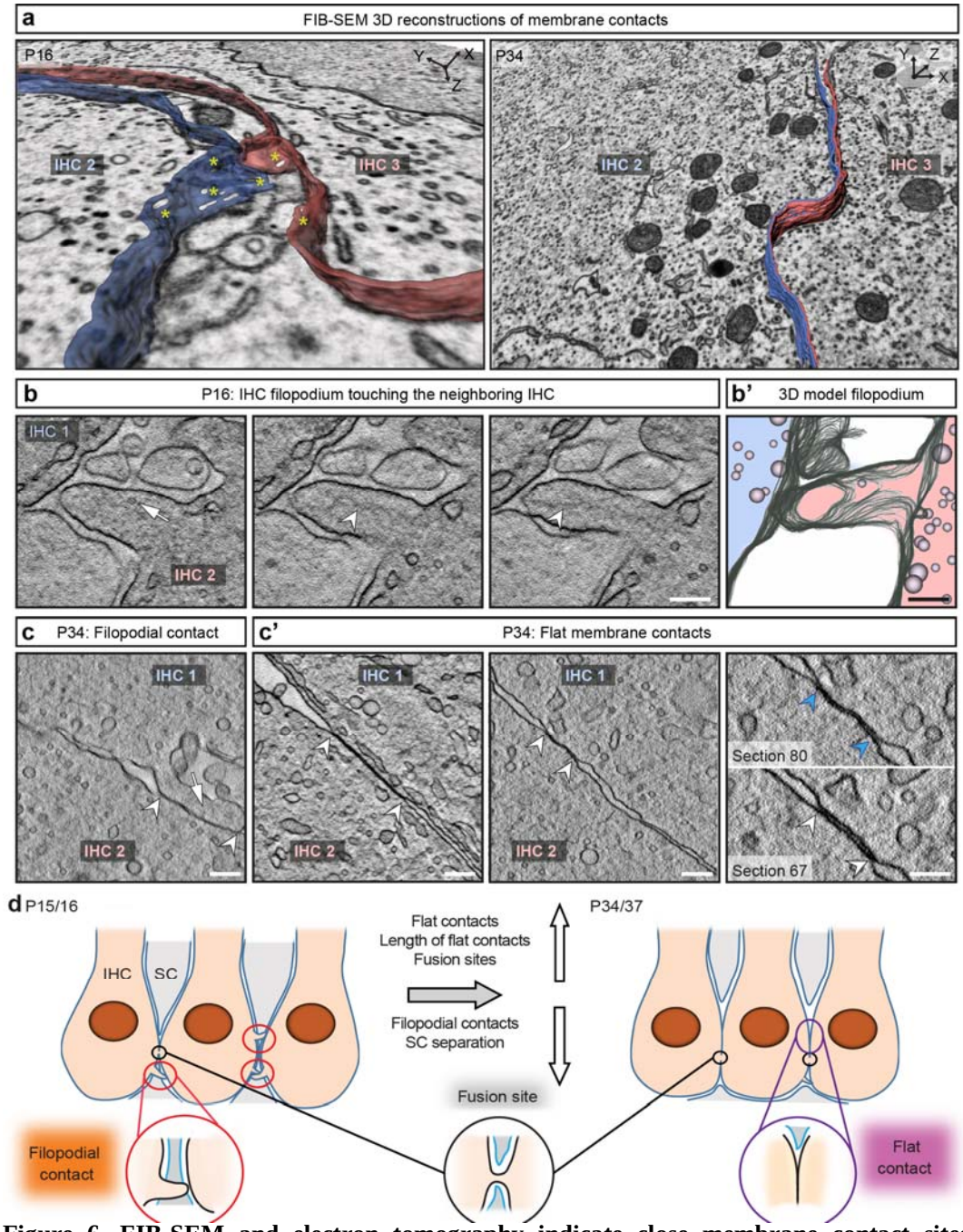

Figure 6. FIB-SEM and electron tomography indicate close membrane contact sites between neighboring IHCs. (a) 3D model of a filopodial contact in immature (P16) IHCs and a flat membrane contact in mature (P34) IHCs. Yellow asterisks highlight regions of non-traceable membrane regions. **(b)** Example tomographic virtual sections from high-pressure frozen/freeze-substituted (HPF/FS) P16 sample showing a filopodium reaching from one IHC to a neighboring IHC (10 virtual sections in z between two pictures, each section distance of 2.616 nm), arrow points to a vesicle, arrowheads to cytoskeletal filaments within filopodium. **(b')** 3D model of the filopodium. **(c)** Example tomographic virtual section from HPF/FS P34 IHCs depicting a filopodium (arrow) between two adjacent cells. The arrowheads indicate the membrane contact. **(c')** Further HPF/FS examples showing two virtual sections of flat IHC-IHC

membrane contacts with different extensions in P34. Right panel: Two virtual sections from the same tomogram as in the middle panel. The membranes come very close and cannot be distinguished anymore in virtual section 80 (blue arrowheads), whereas two separate membranes are visible in section 67 (white arrowheads). **(d)** Schematic illustrating the development of IHC membrane contacts based on the results from FIB-SEM and electron tomography: red circles: filopodial contacts, black circles: fusion sites, purple circles: purple flat membrane contacts. In immature organs of Corti, SCs enwrap the IHCs, while mature IHCs are forming extended flat cell-to-cell membrane contacts. *Abbreviations: FIB-SEM,* focused ion beam-scanning electron microscopy; *IHC,* inner hair cell*; SC,* supporting cell. *Scale bar:* b-c' = 200 nm.

Collective synaptic activity in IHC mini-syncytia

In order to elucidate physiological consequences of IHC coupling, we performed spinning-disk confocal imaging of Ca^{2+}-signals at the individual presynaptic active zones (AZs) in IHC-mini-syncytia. To do so we loaded the mini-syncytium with the low-affinity Ca^{2+} indicator Fluo-4FF, the TAMRA-conjugated CtBP2-binding peptide, and EGTA via the patch-clamped IHC. Under these conditions the Ca^{2+} indicator fluorescence serves as a proxy of synaptic Ca^{2+} influx[19–21]. Depolarization of the patch-clamped IHC evoked Ca^{2+}-signals at the TAMRA-marked AZs within the entire IHC-mini-syncytium (Fig. 7, Fig. S9 for additional examples and Movie S7), likely activating dozens of postsynaptic SGNs. This indicates that SGNs innervating a certain IHC can be activated via the receptor potential shared in the IHC mini-syncytium. We did not find differences of the synaptic Ca^{2+}-signals between the patched IHC (C1) and its coupled neighbor(s) (C2, the number of spots analyzed from further distant coupled cells did not permit statistical comparisons). Neither their maximal amplitude ($\Delta F_{max}/F_0$: 1.48 ± 0.25, n = 37 spots in C1 of 8 mini-syncytia, $N_{animals}$ = 8 vs. 1.88 ± 0.28, n = 43 spots in C2 of 8 mini-syncytia, $N_{animals}$ = 8; p = 0.31, Mann–Whitney–Wilcoxon test) nor their voltage-dependence of activation (V_h: -23.66 ± 2.24 mV, n = 17 spots in C1 in 7 mini-syncytia, $N_{animals}$ = 7 vs. -23.79 ± 1.59 mV, n = 30 spots in C2 in 8 mini-syncytia, $N_{animals}$ = 8; p = 0.96, Student t-test; note that because of signal–to–noise requirements the analysis of voltage-dependence could only be performed on a subset of synapses) were different.

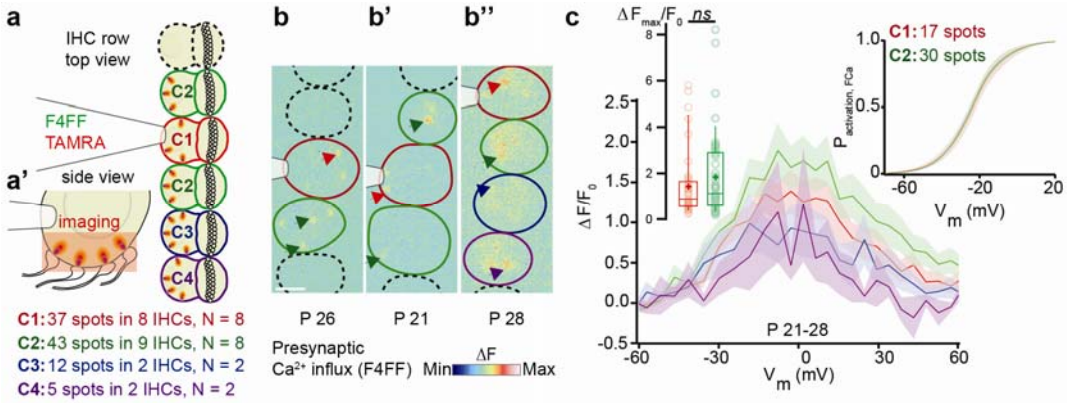

Figure 7. Collective synaptic activity in IHC mini-syncytia. (a) Coupled IHCs (delineated in color) were patch-clamped and loaded with the calcium indicator Fluo-4FF (F4FF) and TAMRA-fluorescent CtBP2-binding peptide. C1 (red) is the patched IHC, C2 (green) are coupled and adjacent to C1, C3 (blue) is coupled to C2 and C4 (violet). **(a')** Red box shows the imaging plane. **(b- b'')** Ca^{2+}-signals co-localizing with the presynaptic ribbons are observable. Example $\Delta F/F_0$ pictures from a single plane of the Ca^{2+}-increments (black arrows) of 2 (b), 3 (b'), and 4 (b'') coupled IHCs. Non-coupled IHCs are delineated in dashed lines. **(c)** The graph displays the fluorescence versus voltage-relationship ($\Delta F/F_0$ versus depolarization level), showing presynaptic activity in the coupled IHCs. Left inset show individual values and percentiles (10th, 25th, 50th, 75th and 90th) of $\Delta F_{max}/F_0$ of synapses in C1 and C2. Means are indicated as crosses. Right inset displays averaged fractional activation curves of a subset of the spots for which the $\Delta F/F_0$ could be fitted faithfully. Mean (line) ± S.E.M. (shaded areas) are displayed. *Abbreviations: IHC*, inner hair cell. *Scale bar:* b-b'' = 5 µm.

Modelling indicates that electrical IHC coupling subtly improves signal-to-noise ratio of sound encoding

Sensory coding, including cochlear sound encoding, is inherently noisy. This noise originates from fluctuations at the transduction and synaptic encoding stages that reflects the stochasticity of ion channels gating and neurotransmitter release. Electrical coupling of sensory cells is expected to attenuate the noise of the receptor potential by averaging the transduction currents of the individual cells. For neighboring IHCs that face a common mechanical input resulting from the sound-driven traveling wave, such electrical intercellular pooling would further reduce fluctuations in mechanotransducer noise at low sound levels.

To test this idea, we used the Neuron simulation environment to model sound encoding at the IHC synapse and signal detection in the cochlear nucleus (CN), where coincident input from several SGNs drives temporally precise spiking of bushy cells (e.g. ref. 22). In the model

(see Supplementary text 1 for details), a deterministic sinusoidal stimulus governs the stochastic gating of mechanotransducer channels in IHCs and the ensuing current drives excursions of the membrane voltage. This receptor potential, in turn, controls Ca^{2+} channel gating (Fig. 8a-e, Fig. S11) and long ($\geq$ 2ms) single Ca^{2+} channel openings are considered to trigger neurotransmitter release events. Pruned by refractoriness, these release events translate to action potentials (APs) in SGNs (Fig. 8f,g, Fig. S11).

The model indicates that signal encoding by presynaptic Ca^{2+} channel openings and postsynaptic AP rates in the cochlea is subtly improved when based on an input coming from SGNs driven by AZs of a mini-syncytium rather than AZs from non-coupled IHCs (see Supplementary text 1 for details). For example, Ca^{2+} channel gating tended to be more representative of the mechanical input in coupled than in non-coupled IHCs (Pearson correlation coefficient: 0.88 for coupled IHCs vs. 0.82 for non-coupled IHCs). Additionally, coincidence signal detection in the CN seemed also slightly improved (2-3%, Fig. S12; Supplementary text 1).

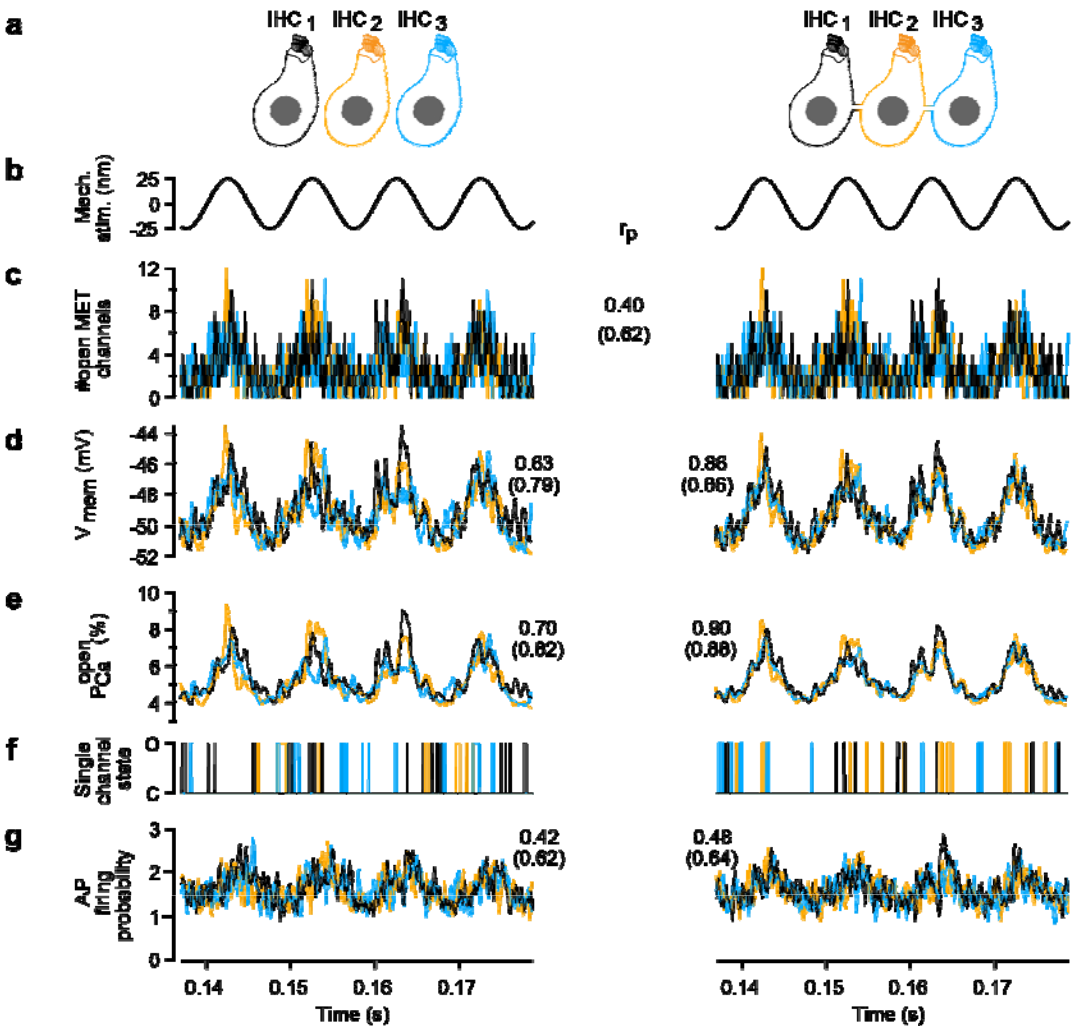

Figure. 8. Electrical IHC coupling coordinates Ca^{2+} channel activity. The signaling steps of IHCs and their synapses, simulated in the Neuron modeling environment for three non-coupled IHCs (left) and three coupled IHCs with a junctional resistance of 25 MOhm (right). **(a)** Simplified representation of IHCs, color-coded for the simulation results presented below. **(b)** Depiction of the sinusoidal mechanical stimulus (identical for all three cells). **(c)** Realization of the stochastic gating of mechanotransducer channels (specific for each cell, identical for coupled and uncoupled cells). **(d)** Membrane voltage variations of the three IHCs. They differ from each other because the mechanotransduction currents differ, but that difference is mitigated by electric coupling (right). **(e)** Illustration of the average open probability, as would result from very many realizations of Ca^{2+} channel gating given the voltage trajectories above. **(f)** Different conductance states (O open, C closed) of one channel in each IHC. **(g)** Modeling stimulus-secretion-coupling and refractoriness for 35,000 independent realizations of (f), an approximate probability to observe an AP in a SGN during a 200 µs window is calculated. Numbers in the central column are Pearson correlation coefficients r_p, averages of correlations between pairs of traces from two different IHCs. In parenthesis are the average correlations between the IHC parameter and the sinusoidal stimulus. For those correlations, time lags of 0.3 ms for the voltage and 0.5 ms for the Ca^{2+}-channels are compensated for. *Abbreviation: AP*, action potential; *IHC*, inner hair cell.

IHC coupling does not degrade frequency resolution of cochlear sound encoding

While IHC coupling appears to be beneficial for sound signal encoding, the fusion of the mechanoreceptive fields of each individual IHC into a larger shared field may lead to poorer sound frequency resolution. To evaluate the effects of IHC coupling on frequency resolution, we estimate that the broadest observed mini-syncytium (9 IHCs) covers approximately 1.29% of the length of the cochlea or 0.06 octaves (see Fig. S13 and Supplementary Text 2 for details). This is less than the physiological estimates of frequency resolution at the level of the basilar membrane (0.17 octaves at the 50-56 kHz region[23]) and auditory nerve fibers (0.37 octaves at the 12 kHz region[24]) of the mouse cochlea. For the human cochlea, we estimate that a single IHC covers approximately 3 cents (1 cent is 1 percent of a semitone, one semitone is 1/12th of an octave) on the tonotopic map of the mid-cochlear quarter of a turn. By assuming that the observed coupling of rodent IHCs also occurs similarly in humans and the whole cochlea is hypothetically formed by tiles of IHC mini-syncytia with the average size of 3 IHCs, the best possible frequency resolution would be 9 cents. This is remarkably close to the lowest psychophysical estimates of frequency resolution (7 cents[25]). Therefore, the low prevalence and small size of mini-syncytia avoids trading off frequency resolution against detection sensitivity.

Discussion

The prevalent view on cochlear sound encoding pictures IHCs as single receptor units that provide sampling of the mechanical stimulus with the highest frequency resolution. In addition, each SGN is believed to receive sensory information from a single IHC. Our results challenge the above views and indicate IHC mini-syncytia to represent auditory receptor fields of the cochlea next to those of uncoupled IHCs. Such patchy information mixing downstream of the mechanical input offers distinct advantages to the system and appears compatible with the frequency resolution of physiological sound encoding. Unlike photoreceptors, IHCs employ GJ-independent coupling. IHC coupling likely arises from cell-to-cell fusion and results in exchange of macromolecules and low resistance electrical connectivity. IHC coupling might be a more general feature of cochlear organization, at least in rodents, as we found it in mice and gerbils, regardless of the tonotopic position.

The mechanism of IHC coupling and its regulation

Based on combining studies of dye diffusion, electrophysiology, and 3D electron microscopy we propose macromolecular IHC coupling via self-limiting cell-to-cell fusion. This seems highly unorthodox at first but it is supported by the unusual coupling properties that are at odds with well-established GJ mechanisms of cell coupling. Firstly, IHC coupling allows the spread of molecules at least as large as fluorophore conjugated antibodies (~150 kDa), exceeding the size limit of GJs (~1 kDa[9]) by two orders of magnitude. Secondly, it offers low resistance electrical connectivity with an average junctional resistance of ~ 35 MOhm. Thirdly, inhibitors of connexins as well as suramin, a blocker of P2X7-dependent, pannexin-containing macropores, failed to prevent dye diffusion and to electrically isolate coupled IHCs. Finally, FIB-SEM provided evidence consistent with IHC-IHC fusion sites at extended contacts formed by their basolateral membranes. The size of the fusion sites, around 50 nm in width and length, seems compatible with the passage of macromalecules or even small organelles. It is also

consistent with single junction resistances of tens to a few hundred MOhm, so that between one and five fusion sites in parallel would result in the experimentally observed junctional resistances of ~35 MOhm. Testing whether fusion sites, indeed, mediate the observed coupling and elucidating their molecular regulation remains another important task for future studies including in IHCs.

What are the molecular mechanisms of the putative IHC-IHC membrane fusion and how could this be limited in space and frequency? We find that the IHC coupling is slowly established after the initiation of hearing function in mice, reaching the prevalence of 30% P30-P45 IHCs forming mini-syncytia consisting of 3 IHCs in average, up to 9 IHCs. We speculate that IHC coupling is a developmentally regulated process, driven by IHC-specific fusogenic machinery, which can take action more efficiently once SCs partially retract from between IHCs. While the identification of the critical molecular components of the machinery regulating such fusion is beyond the scope of the present study, future work could consider manipulating the function of myosin X [26] expressed in IHCs[27]. Additionally, other molecules involved in the formation of tunneling membrane nanotubes might also operate in putative IHC-IHC membrane fusion.

As cell fusion has been reported to occur in neural cells upon cellular damage[3] and our data have been obtained from *ex vivo* preparations of the cochlea, artefactual IHC fusion needs to be considered. Several lines of evidence argue against tissue damage as the cause of IHC coupling. Cell injury related to tissue handling would be expected to also induce fusion of IHCs to SCs. As we never observed dye spread from IHC to SCs, the molecular coupling is specific to IHCs (homotypic coupling). IHC recordings revealing Ca^{2+} current amplitudes worth multiples of the single IHC Ca^{2+} current were also observed 20 min *post-mortem* in the ruptured-patch clamp configuration without removing the contacting SCs (Fig. S3). Therefore, IHC coupling was not simply induced by potential cellular stress associated with rupturing the cell membrane and removing adjacent structures. Resting currents, a sensitive parameter reflecting cell health, was not significantly different between non-coupled IHCs before and from P28 in our

recordings from the excised gerbil organ of Corti (p = 0.47; data not shown). This argues that increased probability of IHC coupling in the more mature preparation does not reflect compromised IHC health in the older preparations. In a temporal bone preparation, which require little dissection of the cochlea and maintains its integrity in a near-physiological state, IHC coupling was observed 15 min *post-mortem*. Moreover, during up to one-hour long patch clamp recordings we never observed an IHC spontaneously becoming coupled to a previously non-coupled neighboring IHC. This indicates that *ex vivo* conditions as artificial as a long-lasting ruptured-patch recording do not readily induce IHC coupling. Direct demonstration that IHC coupling exists *in vivo* is a challenging task, as cell-level recording and imaging methods typically require the opening of the cochlea. Therefore, new approaches will be required to probe IHC coupling *in vivo*.

The physiological implications of IHC coupling

What then are the physiological implications of IHC mini-syncytia interspersed between non-coupled IHCs along the tonotopic axis of the organ of Corti? Coupling into mini-syncytia confers considerable advantages for sharing of metabolites and potentially even organelles between cells. As adult mammals cannot regenerate functional IHCs, IHCs must survive and remain functional for a lifetime – otherwise sensorineural hearing loss develops. By being able to share metabolites and a joint Ca^{2+}-buffering capacity, coupled IHCs can potentially withstand higher levels of cellular stress than a single IHC alone. On the other hand, initiation of cell death processes in one of the coupled IHCs puts all of them in danger if the macromolecular coupling cannot be terminated. Future studies should test the implications of IHC coupling to cell survival.

Beyond the advantage for IHCs, our study indicates that coupling also benefits the sound encoding by SGNs. Patch-clamp combined with Ca^{2+} imaging demonstrated a collective response of the presynaptic AZs within the IHC mini-syncytium, wherein the maximal amplitude and voltage-dependence of the AZs of the patched and the neighboring cells were not

different. While the activation time course of the collective Ca^{2+} current suggests minimal if any temporal delays in recruiting the AZs, scrutinizing the synchrony of synaptic transmission in future experiments remains an important task. Regardless of the degree of synchrony, for slowly fluctuating stimuli the shared receptor potential would govern the release at all AZs. Then, a single SGN encodes information on mechanical stimuli sensed and averaged across the IHCs of the mini-syncytium, even though it receives transmission only from one AZ of one IHC. A coupled IHC with stereociliar damage could still be driven by the shared receptor potential of the mini-syncytium, such that the SGNs postsynaptic to this IHC can contribute to sound encoding provided a fit neighbor.

Comparing sound encoding in conditions with and without the coupling described here for rodent IHCs will be instrumental to experimentally probe the advantage predicted by the computational model (Fig. 8). Ideally, such studies could be performed in the same species, e.g. in mice with genetic disruption of IHC coupling and will help to validate the notion that the low prevalence and small size of mini-syncytia avoids degradation of the frequency resolution of sound coding. Beyond this, the possible existence in other mammals remains to be studied. For example, it will be interesting to see whether IHCs inside the "acoustic fovea" of certain mole rats[28], owls[29], and echo-locating bats[30] are coupled; proposing an additional cellular candidate mechanism for this enigmatic phenomenon.

REFERENCES

1. Shepherd, G. M. *Foundations of the Neuron Doctrine: 25th Anniversary Edition*. (Oxford University Press, 2015).
2. Oren-Suissa, M., Hall, D. H., Treinin, M., Shemer, G. & Podbilewicz, B. The Fusogen EFF-1 Controls Sculpting of Mechanosensory Dendrites. *Science* **328**, 1285–1288 (2010).
3. Giordano-Santini, R., Linton, C. & Hilliard, M. A. Cell-cell fusion in the nervous system: Alternative mechanisms of development, injury, and repair. *Semin. Cell Dev. Biol.* **60**, 146–154 (2016).

4. Alcamí, P. & Pereda, A. E. Beyond plasticity: the dynamic impact of electrical synapses on neural circuits. *Nat. Rev. Neurosci.* **20**, 253–271 (2019).
5. Harris, A. L. Electrical coupling and its channels. *J. Gen. Physiol.* **150**, 1606–1639 (2018).
6. Connors, B. W. & Long, M. A. ELECTRICAL SYNAPSES IN THE MAMMALIAN BRAIN. *Annu. Rev. Neurosci.* **27**, 393–418 (2004).
7. Bloomfield, S. A. & Völgyi, B. The diverse functional roles and regulation of neuronal gap junctions in the retina. *Nat. Rev. Neurosci.* **10**, 495–506 (2009).
8. Christie, J. M. & Westbrook, G. L. Lateral Excitation within the Olfactory Bulb. *J. Neurosci.* **26**, 2269–2277 (2006).
9. Mammano, F. Inner Ear Connexin Channels: Roles in Development and Maintenance of Cochlear Function. *Cold Spring Harb. Perspect. Med.* (2018) doi:10.1101/cshperspect.a033233.
10. Kiang, N. Y., Rho, J. M., Northrop, C. C., Liberman, M. C. & Ryugo, D. K. Hair-cell innervation by spiral ganglion cells in adult cats. *Science* **217**, 175–177 (1982).
11. Fettiplace, R. Hair Cell Transduction, Tuning, and Synaptic Transmission in the Mammalian Cochlea. *Compr. Physiol.* **7**, 1197–1227 (2017).
12. Mikaelian, D. & Ruben, R. J. Development of Hearing in the Normal Cba-J Mouse: Correlation of Physiological Observations with Behavioral Responses and with Cochlear Anatomy. *Acta Otolaryngol. (Stockh.)* **59**, 451–461 (1965).
13. Juszczak, G. R. & Swiergiel, A. H. Properties of gap junction blockers and their behavioural, cognitive and electrophysiological effects: Animal and human studies. *Prog. Neuropsychopharmacol. Biol. Psychiatry* **33**, 181–198 (2009).
14. Shimamura, K. *et al.* Effects of flufenamic acid on smooth muscle of the carotid artery isolated from spontaneously hypertensive rats. *J. Smooth Muscle Res. Nihon Heikatsukin Gakkai Kikanshi* **38**, 39–50 (2002).
15. Squecco, R., Bencini, C., Piperio, C. & Francini, F. L-type Ca2+ channel and ryanodine receptor cross-talk in frog skeletal muscle. *J. Physiol.* **555**, 137–152 (2004).

16. Vessey, J. P. *et al.* Carbenoxolone Inhibition of Voltage-Gated Ca Channels and Synaptic Transmission in the Retina. *J. Neurophysiol.* **92**, 1252–1256 (2004).

17. Qiu, F. & Dahl, G. A permeant regulating its permeation pore: inhibition of pannexin 1 channels by ATP. *Am. J. Physiol. - Cell Physiol.* **296**, C250–C255 (2009).

18. Rustom, A., Saffrich, R., Markovic, I., Walther, P. & Gerdes, H.-H. Nanotubular highways for intercellular organelle transport. *Science* **303**, 1007–1010 (2004).

19. Jean, P. *et al.* The synaptic ribbon is critical for sound encoding at high rates and with temporal precision. *eLife* **7**, (2018).

20. Neef, J. *et al.* Quantitative optical nanophysiology of Ca 2+ signaling at inner hair cell active zones. *Nat. Commun.* **9**, 290 (2018).

21. Ohn, T.-L. *et al.* Hair cells use active zones with different voltage dependence of Ca2+ influx to decompose sounds into complementary neural codes. *Proc. Natl. Acad. Sci.* **113**, 201605737 (2016).

22. Joris, P. X., Carney, L. H., Smith, P. H. & Yin, T. C. Enhancement of neural synchronization in the anteroventral cochlear nucleus. I. Responses to tones at the characteristic frequency. *J. Neurophysiol.* **71**, 1022–1036 (1994).

23. Lukashkina, V. A., Levic, S., Lukashkin, A. N., Strenzke, N. & Russell, I. J. A connexin30 mutation rescues hearing and reveals roles for gap junctions in cochlear amplification and micromechanics. *Nat. Commun.* **8**, 14530 (2017).

24. Taberner, A. M. & Liberman, M. C. Response Properties of Single Auditory Nerve Fibers in the Mouse. *J. Neurophysiol.* **93**, 557–569 (2005).

25. He, N., Dubno, J. R. & Mills, J. H. Frequency and intensity discrimination measured in a maximum-likelihood procedure from young and aged normal-hearing subjects. *J. Acoust. Soc. Am.* **103**, 553–565 (1998).

26. Gousset, K., Marzo, L., Commere, P.-H. & Zurzolo, C. Myo10 is a key regulator of TNT formation in neuronal cells. *J. Cell Sci.* **126**, 4424–4435 (2013).

27. Liu, H. *et al.* Characterization of transcriptomes of cochlear inner and outer hair cells. *J. Neurosci. Off. J. Soc. Neurosci.* **34**, 11085–11095 (2014).

28. Müller, M., Laube, B., Burda, H. & Bruns, V. Structure and function of the cochlea in the African mole rat (Cryptomys hottentotus): evidence for a low frequency acoustic fovea. *J. Comp. Physiol. [A]* **171**, 469–476 (1992).

29. Köppl, C., Gleich, O. & Manley, G. A. An auditory fovea in the barn owl cochlea. *J. Comp. Physiol. A* **171**, 695–704 (1993).

30. Bruns, V. & Schmieszek, E. Cochlear innervation in the greater horseshoe bat: demonstration of an acoustic fovea. *Hear. Res.* **3**, 27–43 (1980).